Check for updates

View Article Online
View Journal

Analyst

Accepted Manuscript

This article can be cited before page numbers have been issued, to do this please use: A. Gupta, G. Dorlhiac and A. M. Streets, *Analyst*, 2018, DOI: 10.1039/C8AN01525B.

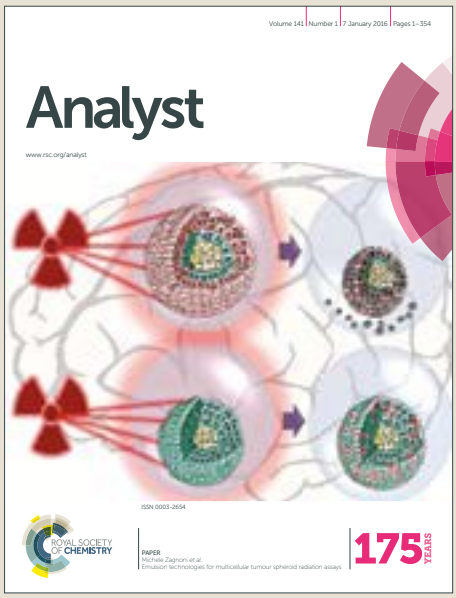

This is an Accepted Manuscript, which has been through the Royal Society of Chemistry peer review process and has been accepted for publication.

Accepted Manuscripts are published online shortly after acceptance, before technical editing, formatting and proof reading. Using this free service, authors can make their results available to the community, in citable form, before we publish the edited article. We will replace this Accepted Manuscript with the edited and formatted Advance Article as soon as it is available.

You can find more information about Accepted Manuscripts in the author guidelines.

Please note that technical editing may introduce minor changes to the text and/or graphics, which may alter content. The journal's standard Terms & Conditions and the ethical guidelines, outlined in our author and reviewer resource centre, still apply. In no event shall the Royal Society of Chemistry be held responsible for any errors or omissions in this Accepted Manuscript or any consequences arising from the use of any information it contains.

ROYAL SOCIETY OF CHEMISTRY

rsc.li/analyst

View Article Online
DOI: 10.1039/C8AN01525B

Published on 17 October 2018. Downloaded by University of California - Berkeley on 10/17/2018 9:25:16 PM.

Quantitative imaging of lipid droplets in single cells

Gupta Anushka[1], Dorlhiac Gabriel F[2] and Streets Aaron M[*1,2,3]
[1]UC Berkeley-UC San Francisco Graduate Program in Bioengineering, University of California, Berkeley Graduate Division, Berkeley, California
[2] Biophysics Graduate Group, University of California, Berkeley, California
[3]Chan Zuckerberg Biohub, San Francisco, California

Abstract:

The combination of next generation sequencing (NGS) and automated liquid handling platforms has led to a revolution in single-cell genomic studies. However, many molecules that are critical to understanding the functional roles of cells in a complex tissue or organ, are not directly encoded in the genome, and therefore cannot be profiled with NGS. Lipids, for example, play a critical role in many metabolic processes but cannot be detected by sequencing. Recent developments in quantitative imaging, particularly coherent Raman scattering (CRS) techniques, have produced a suite of tools for studying lipid content in single cells. This article reviews CRS imaging and computational image processing techniques for non-destructive profiling of dynamic changes in lipid composition and spatial distribution at the single-cell level. As quantitative CRS imaging progresses synergistically with microfluidic and microscopic platforms for single-cell genomic analysis, we anticipate that these techniques will bring researchers closer towards combined lipidomic and genomic analysis.

1. Introduction

While each cell in an organism has essentially the same genome, variation in gene regulation gives rise to vast cellular heterogeneity. This heterogeneity is present in tissues and even among populations of cells of the same type. Cellular heterogeneity plays an important role in many biological processes, including cell fate determination,[1,2] cancer development and relapse,[3,4] and drug resistance.[5] Investigations at the single-cell level are therefore critical for uncovering this heterogeneity which otherwise is masked by ensemble measurements. Many single-cell analysis techniques have been enabled by next generation sequencing (NGS). Reverse transcription of mRNA followed by high-throughput sequencing of cDNA (RNA-sequencing) allows transcriptome-wide gene expression profiling. Recently, microfluidic platforms have made it possible to isolate mRNA from hundreds to thousands of single cells in a single experiment, thereby enabling comprehensive mapping of cellular composition of biological tissues and organs. These technological advances have paved the way towards constructing a human cell atlas.[6] The Human Cell Atlas project[7] aims to leverage high-throughput single-cell RNA sequencing (scRNA-seq) along with other single-cell measurements, to quantitatively characterize cellular identity throughout the human body, tracking both developmental and disease states, within their contextual niche. Recent work has already composed transcriptional catalogues of both mouse and human organs, including the brain,[8,9] the thymus,[10] the pancreas,[11] and two recent reports of a comprehensive mouse atlas.[12,13]

While scRNA-seq has proven to be a robust tool for quantifying cellular identity, there are many molecules, which play critical roles in cellular function, that are not directly encoded in the genome and therefore cannot be detected with measurements that are based on sequencing. Metabolites and lipids are examples of such molecules that cannot be profiled using NGS but are important for regulation of cellular function. Lipids are predominantly involved in energy storage in cells and provide

Analyst Accepted Manuscript

View Article Online
DOI: 10.1039/C8AN01525B

Published on 17 October 2018. Downloaded by University of California - Berkeley on 10/17/2018 9:25:16 PM.

structural integrity to biological membranes.[14,15] Lipids also participate in signaling pathways[14,16] and interact with proteins to regulate their functions.[17,18] In cells, neutral lipids and phospholipids are stored in organelles called lipid droplets (LDs). For a long time, LDs' only role was perceived as storage of lipids.[19] It is now well-accepted that LDs are dynamic organelles with functions in energy production,[20] protein degradation,[21] and lipid metabolism homeostasis.[22] The dysregulation of lipid metabolism has been linked to many human diseases such as cancer, obesity, and diabetes. For example, imbalance in the number of intracellular LDs has been reported to be associated with multiple cancers[23] and has been shown to promote cancer progression.[24] Obesity is associated with eventual accumulation of lipids in nonadipose tissues[25,26] which subsequently interferes with local insulin signaling and plays a key role in the development of type II diabetes.[27] Consequently, quantifying changes in lipid metabolism is critical for understanding disease pathways and screening for targeted therapeutics.[28,29]

There are many different species of cellular lipids with structural variations in their hydrophobic and hydrophilic regions. Intracellular LDs store a wide distribution of lipid molecules and lipid metabolism directly alters the lipid composition of LDs.[30,31] The field of lipidomics aims to study changes in lipid metabolism in response to physiological, pathological, and environmental conditions by characterizing this compositional distribution of all cellular lipids.

Established techniques for lipidomic analysis include gas or liquid chromatography-mass spectrometry (GC/LC-MS)[32-34] and shotgun mass spectrometry.[35,36] GC/LC-MS and shotgun techniques allow for targeted and untargeted detection of lipid molecules, respectively, when implemented on biological extracts from a population of cells (Fig. 1A). Recent advancements in sample preparation and ionization techniques have further enabled researchers to profile the lipidome at the single-cell level based on microarray for MS (MAMS), single-cell matrix assisted laser desorption/ionization-MS (MALDI-MS), and subcellular content aspiration-based MS techniques.[37-40] Imaging mass spectrometry (IMS) is an imaging method that allows for visualization and quantification of spatial distribution of lipids in intact biological systems.[41-45] Implementation of IMS techniques requires extensive sample preparation[46] with spatial resolution ranging from submicron to hundreds of microns depending on the ion source.[47] Typically, sensitivity of MS-based techniques lies in the picomolar range with detection specificity of hundreds of lipid species simultaneously.[48] Such high sensitivity and specificity of MS-based techniques comes at the cost of destructive measurements.

Quantitative microscopic imaging techniques are complementary to MS-based technology and allow for non-destructive spatial characterization of LDs in live cells but with less lipid specificity. The non-destructive nature of optical microscopy allows researchers to perform time-resolved imaging to investigate dynamic cellular behavior. Furthermore, live-cell imaging can be coupled with subsequent molecular measurements such as sequencing or mass-spectrometry. Also, when combined with image processing algorithms, microscopy enables researchers to gather subcellular information such as LD morphology, or LD composition. This circumvents the need for physical isolation of single cells, thereby increasing the speed of data acquisition (Fig. 1B).

Amongst quantitative microscopic imaging techniques, fluorescence imaging allows for quantification down to a single molecule level. Fluorescence imaging with lipid-soluble dyes, lipid-binding probes, or fluorophore-conjugated lipids, has been used to study the composition and morphology of LDs.[49,50] In some cases, the process of labeling can alter the distribution of cellular lipids. For example, Yen *et al.* showed that staining based on both Nile red and BODIPY does not correlate with fat stores for the model organism *C. elegans*.[51] Complementary to fluorescence imaging are label-free optical

Analyst Accepted Manuscript

View Article Online
DOI: 10.1039/C8AN01525B

Published on 17 October 2018. Downloaded by University of California - Berkeley on 10/17/2018 9:25:16 PM.

techniques such as phase contrast,[52] differential interference contrast,[53] quantitative phase-imaging,[54] and third harmonic generation microscopy[55] that have been used to visualize LDs. In order to extend the capabilities of label-free imaging techniques for lipid profiling and quantification, magnetic resonance imaging (MRI) and coherent Raman scattering (CRS) techniques have been implemented to provide a lipid-specific contrast. MRI is an imaging technique based on nuclear magnetic resonance that has been implemented for quantification of total fat content and lipid accumulation.[56-58] The high penetration depth achieved from near-IR imaging allows researchers to implement MRI techniques *in vivo*. For *in vitro* and *in vivo* label-free mapping of LD composition, CRS imaging techniques are used. CRS techniques include coherent anti-Stokes Raman scattering (CARS) imaging and stimulated Raman scattering (SRS) imaging, both of which have been widely used to quantify LDs at the single-cell level with high spatial and temporal resolution. In this review, we will highlight applications of CRS techniques for quantifying LDs. We will also discuss object recognition algorithms for identification of LD and cellular boundaries in an image. Such segmentation analysis is necessary for microscopy to be used for quantitative single-cell analysis. We will conclude by discussing the implications of non-destructive CRS techniques towards promises of multi-omic analysis at the single-cell level.

2. Coherent Raman Scattering (CRS) Microscopy

CRS microscopy provides a label-free approach for profiling the chemical composition of biological specimens by probing the characteristic vibrational modes of molecular bonds. Because of the strong vibrational modes associated with CH_2, CRS is particularly powerful for imaging intracellular lipids. For selective imaging of lipids, the asymmetric-stretching vibrational mode of the carbon–hydrogen bond is probed at 2,845 cm^{-1} (Fig. 2A). CRS is induced by simultaneously illuminating the specimen with two photons at frequencies ω_p (pump) and ω_s (Stokes). When the difference in frequency between the two photons equals a vibrational frequency that is characteristic of the target molecule ($\Omega = \omega_p - \omega_s$), the Raman scattering cross-section is resonantly enhanced giving rise to a strong CRS signal. Coherent anti-Stokes Raman scattering (CARS) and stimulated Raman scattering (SRS) are two imaging modalities that operate on this principle. In CARS, a signal is detected at the anti-Stokes frequency, ω_{AS}, given by $\omega_{AS} = 2\omega_p - \omega_s$. CARS relies on homodyne detection, as ω_{AS} can be separated from both the incoming frequencies ω_p and ω_s using a dichroic mirror or optical filters.[59] In SRS, one of the two incoming photons, ω_s or ω_p, is amplitude modulated and the signal is detected as a loss or gain in the intensity of the pump or Stokes photon respectively (Fig. 2B). Therefore, SRS techniques utilize heterodyne detection schemes and require a lock-in amplifier to amplify the modulated stimulated Raman loss or gain.[60] As CARS and SRS are nonlinear optical processes, signal is only generated at the focal plane of the objective, enabling intrinsic three-dimensional sectioning by scanning in the *x*, *y*, and *z* axes. Long-term live cell imaging is also possible as CRS contrast is not limited by photobleaching. CARS and SRS are diffraction limited techniques and therefore offer quantification at a subcellular level with resolution as low as hundreds of nanometers. The CARS signal is quadratic with respect to the concentration of resonant chemical bonds and the SRS signal is linear. SRS also has a higher signal to noise ratio (SNR) as compared to CARS because there is no non-resonant background. However, heterodyne detection in SRS requires additional instrumentation (lock-in amplifier) which is bypassed in CARS by using appropriate filters for homodyne detection.

Multiphoton excitation techniques like CRS imaging employ ultrashort pulsed lasers to obtain high concentrations of laser power inside the sample, which is necessary for efficient excitation of the targeted vibrational mode. A possible consequence of this elevated laser irradiance is photodamage to cells and tissues. Schönle and Hell developed a model for investigating the effects of optical absorption

Analyst Accepted Manuscript

View Article Online
DOI: 10.1039/C8AN01525B

Published on 17 October 2018. Downloaded by University of California - Berkeley on 10/17/2018 9:25:16 PM.

(in near-IR, by water in biological specimens) on focal heating during multiphoton excitation microscopy.[61] Their results showed an increase in focal temperature by not more than 3K for an average laser power of 100 mW at the focal plane, suggesting that heating through linear absorption does not play a destructive role. However, the required peak laser power, to maintain an average laser power of 100 mW, may lead to nonlinear photodamage. Other studies have shown that maintaining laser power below 10 mW at the focal plane is considered to be a safe range for sample integrity.[62,63] Some applications of CRS imaging may require higher laser power for fast and efficient excitation of the resonant mode.[64,65] For such purposes, optimizing the average and peak laser power should be the first step towards maintaining a strong signal while minimizing photodamage to the sample.[66] Work has been done by several research groups to identify and define criterias for characterization of photodamage induced by nonlinear imaging.[67-70]

In this section, we discuss investigations using CRS techniques for quantifying LDs. In section 3, we will then discuss object recognition algorithms applicable for cell and LD boundary determination. Section 4 will focus on biological investigations using CRS techniques coupled with segmentation algorithms for quantitative single-cell and single-lipid droplet analysis.

2.1. CARS and SRS

As CARS signal is quadratic with molecular concentration of the resonant bond, quantification using CARS requires processing of signal intensity. For example, Chen *et al.* derived a formula to calibrate CARS intensity to accurately report the number of lipid molecules in the scattering volume.[71] In this study, they developed an automated image analysis algorithm for quantification of lipid content in single cells. Rinia *et al.* adopted another strategy where they implemented spectral-analysis tools in conjunction with multiplex CARS for retrieval of spontaneous Raman-like spectra which is linear with the number of vibrating molecules.[72] In this study, they analyzed the retrieved spontaneous Raman-like spectra to map the acyl chain unsaturation and acyl chain order within individual LDs in adipocytes, which were incubated with exogenous free fatty acids (FFA) of varying compositions (Fig. 3). They found heterogeneity in lipid composition and packing in individual LDs and demonstrated that this heterogeneity was dependent on the FFA composition of incubation mixture. In contrast to CARS, SRS signal is linear with the number of vibrating molecules, thereby making quantification more straightforward. Freudiger *et al.* demonstrated SRS as a contrast mechanism for imaging biological specimens.[60] They monitored the uptake and metabolism of unsaturated FFA by imaging at 3015 cm^{-1} wavenumber specific to the =C-H bond in unsaturated fatty acids. Wang *et al.* used SRS microscopy combined with RNA interference screening to determine lipid storage regulatory genes in *C. elegans*.[73] Lipid storage capacity was quantified based on mean SRS intensity. Using this technique, they were able to screen for 272 genes and found 8 new regulatory genes for fat storage. Besides quantifying LDs, CRS techniques have been critical towards visualizing LD growth and formation thereby revealing new lipid functions in cellular environment.[74,75] Nan *et al.* demonstrated vibrational imaging of LDs using CARS and monitored LD formation during differentiation of 3T3-L1 fibroblast cells into adipocytes.[76] They found that after adding adipogenic differentiation media, there was an initial clearance of LDs at the early stage of differentiation followed by formation of large LDs (Fig. 4). Le and Cheng combined CARS microscopy with fluorescence imaging and flow cytometry to investigate heterogeneity in rates of LD formation in differentiating 3T3-L1 cells.[77] They found that phenotypic variability among differentiating 3T3-L1 cells was dependent on the kinetics of an insulin signaling cascade.

2.2. Vibrational Raman tags

Analyst Accepted Manuscript

View Article Online
DOI: 10.1039/C8AN01525B

Published on 17 October 2018. Downloaded by University of California - Berkeley on 10/17/2018 9:25:16 PM.

Imaging at a single frequency is insufficient for monitoring the uptake of saturated fatty acids because all vibrational markers of saturated fatty acids are shared by unsaturated fatty acids. However, no endogenous molecular species, including lipids, vibrate in the range from 1800 cm^{-1} to 2800 cm^{-1}, known as the "Raman-silent region" in cells. Raman tags are biorthogonal vibrational labels that consist of chemical bonds having a unique Raman shift in the cell's silent region. Fatty acids have been conjugated with Raman tags for tracking their uptake dynamics. Stable isotope substitution using ^2H[78,79] or conjugation with alkyne tags[80,81] are the two major strategies employed with CRS techniques. Wei *et al.* demonstrated metabolic incorporation of saturated FFA into triglycerides and its storage in LDs using alkyne tagging together with SRS.[82] Li and Cheng demonstrated direct visualization and quantification of glucose metabolism in single cells using SRS microscopy coupled with isotope labeling (glucose-d_7).[83] They demonstrated up-regulation of *de novo* lipogenesis in pancreatic and prostate cancer cell lines as compared to healthy cell lines. They also showed that compared to pancreatic cancer cells, prostate cancer cells have lower level of *de novo* lipogenesis but higher level of dietary lipid uptake. On the other hand, Hu *et al.* monitored glucose uptake activity in live cells using a glucose analogue labeled with an alkyne tag (3-O-propargyl-d-glucose, 3-OPG).[84] In their study, they found that glioblastoma cells have a higher level of *de novo* lipogenesis as compared to cervical cancer cells. These studies demonstrated that cancer cells with differing metabolic activities can be distinguished using Raman tagging strategies. It will be interesting to see if the reported results can be validated for prostate and pancreatic cells using alkyne tagging and for cervical and glioblastoma cells using isotope labeling.

2.3. Hyperspectral SRS

Single-channel imaging of deuterated or alkyne-tagged lipids has been demonstrated as a useful tool for tracking uptake dynamics of a targeted lipid molecule. For unbiased profiling of the distribution of cellular lipids in response to changes in cellular metabolic states, hyperspectral SRS (hSRS) imaging is implemented. hSRS imaging enables researchers to separately quantify lipid molecules with overlapping Raman spectra by utilizing subtle differences in the spectral intensity across a range of wavenumbers.[85,86] hSRS techniques are often used in conjunction with spectral-analysis tools to retrieve the Raman spectra of different molecules from the convoluted SRS spectra. The retrieved spectra can be used to reconstruct the compositional distribution images for each lipid species (Fig. 5).[87,88] Li *et al.* employed hSRS imaging to quantitatively analyze the composition of intracellular lipids inside single ovarian cancer and non-cancer stem cells and reported higher levels of unsaturated lipids in cancer cells based on the ratio of intensities at 3002 cm^{-1} and 2900 cm^{-1} wavenumber.[89] Alfonso-García *et al.* used hSRS coupled with unsupervised vertex component spectral analysis to study the metabolism and storage of deuterated cholesterol (D38-cholesterol).[90] They utilized the spectral differences in the CH fingerprint region between D38-cholesterol and natural cholesterol to map the distribution of esterified and unesterified cholesterol in LDs. They found that subpopulations of LDs exist each with a predominant storage of esterified or free cholesterol. They also found that steroidogenic Y1 cells store triacylglycerol (TAG) and cholesteryl esters (CE) in different LDs. It is known that steroidogenic cells and macrophages primarily accumulate CE in LDs and liver cells primarily accumulate TAG in LDs.[91,92] This study observed accumulation of TAG in steroidogenic cells but didn't perform any investigation in macrophages or liver cells.[90] In contrast, Fu *et al.* detected only CE containing LDs in macrophages and only TAG containing LDs in hepatocytes.[93] In this study, spectral differences between TAG and CE were utilized to quantitatively profile the two classes of neutral lipids. Based on these observations, it will be interesting to see whether lipid sorting occurs in macrophages, liver cells and other cell types using Alfonso-García's methodology. Fu *et al.* also

Analyst Accepted Manuscript

View Article Online
DOI: 10.1039/C8AN01525B

Published on 17 October 2018. Downloaded by University of California - Berkeley on 10/17/2018 9:25:16 PM.

characterized lipid compositional changes associated with metabolic disorders and further extended hSRS coupled with isotope labeling to simultaneously trace saturated and unsaturated fatty acids.[93]

3. Object Recognition Algorithms

While optical microscopy has the spatial resolution necessary to be an inherently single-cell measurement, interpretation of micrographs in the single-cell paradigm is not always straightforward. Historically, microscopy has been used in low volume, manual, and generally qualitative, descriptions of biological samples. Such an approach, in addition to being susceptible to interpretation bias, is now increasingly impractical as image data has become larger and more complex. Furthermore, with the push in the life sciences towards generating results with greater statistical power, there is more demand for quantitative analyses of images, which all but necessitates computation. Image analysis algorithms have been under development since the pre-digital age, and the past two decades have seen many improvements in their application to biological datasets.

One of the most basic, and arguably most important, questions that can be asked about an image is where are the boundaries between objects? When quantifying metabolic composition of cells, it is important to have an objective methodology for defining objects. In tissue this amounts to cell boundaries, in individual cells, the subcellular structures and organelles such as LDs. Traditional techniques for answering this question often start with contrast enhancement and gradient-based edge detection methods. The simplest approach is thresholding, with automatic threshold determination by algorithms such as Otsu's method,[94] or balanced histogram thresholding.[95] Thresholding tends to separate objects and is also often employed to aid in background correction. Convolution with operators such as the Sobel,[96] Canny,[97] or other gradient operators can provide information on sharp line boundaries. For more general shape extraction, the Hough transform has been a popular choice in a wide variety of fields. First patented in 1962 for line identification,[98] it was then generalized to arbitrary shapes.[99] It is well-suited to identifying regularly shaped features which can vary in dimension across an image.

These gradient or edge detection techniques are then frequently combined with a watershed-based algorithm,[100] which imagines filling basins from minima in the images and draws boundaries where the watersheds meet. Implementations of these techniques can be found in all major programming languages, and are also included in many widely available image analysis software suites, like Fiji.[101] They have therefore been applied, in a number of combinations and variations, for analysis of LD size and number distribution.[102,103]

More recently, the field of computer vision has shifted focus to machine learning approaches for everything from automatic feature extraction to image classification. This has been driven in large part by the success of convolutional neural networks (CNN), and their rapid development in the past decade. First introduced over 20 years ago,[104,105] initial adoption was slow, but the list of current variations and applications is now constantly growing. CNNs work similarly to conventional, or 'fully-connected,' neural networks but reduce the number of parameters that need to be learned by using convolutions rather than transformation matrices that relate every point in the image to every point in the output. This is in some ways analogous to some traditional methods listed above, but instead of pre-selecting, e.g. a gradient filter, the filter is learned by the network, and there are many filtering steps. While generally more computationally intensive, fully-connected neural networks have also found use in image analysis.

Analyst Accepted Manuscript

View Article Online
DOI: 10.1039/C8AN01525B

Published on 17 October 2018. Downloaded by University of California - Berkeley on 10/17/2018 9:25:16 PM.

The major drawback for using CNNs or deep learning architectures generally is the need for training data. This has slowed adoption in the field of lipidomics, although CNNs have been successfully applied to numerous types of microscopy data. Medical imaging has been a recent adopter, with hundreds of successful demonstrations in the last three years.[106] Importantly, these demonstrations span a wide-variety of disciplines but utilize similar network architectures. Many are straightforward modifications of well-known networks, and often rely on already trained networks as starting points, suggesting a similar strategy may be effective for lipidomics. Single-cell segmentation, cell cycle progression and disease state identification, have been recently demonstrated using CNNs on fluorescent images.[107] Chen *et al.* also recently showed algal cell classification based on lipid content, using time-stretch quantitative phase imaging and deep neural networks.[108]

A final consideration, is that many of the imaging techniques used for lipid characterization contain additional information beyond the purely morphological. Most of the analysis algorithms discussed thus far have focused on segmentation and object identification. This makes them generalizable to all types of images, but also makes them blind to the additional information that can be encoded in some microscopy datasets. In some cases, it is therefore advantageous to utilize more specialized algorithms for analysis, hyperspectral coherent Raman imaging being a prime example. Fu and Xie demonstrated the ability to segment subcellular structures, including lipid droplets, from a hSRS dataset using a spectral phasor method adapted from the fluorescence lifetime imaging field.[109] Di Napoli *et al.* were also able to monitor uptake of different lipid components using hyperspectral CARS,[110] using an unsupervised retrieval algorithm.[111]

4. Quantitative CRS for single-cell and single-LD analysis

High signal to noise ratio (SNR) associated with concentrated CH_2 bonds in lipids allows researchers to monitor the dynamics of LDs in a straightforward fashion using CRS techniques coupled with LD recognition and trajectory tracking packages. Jungst *et al.* demonstrated tracking of LDs using fast, long-term three-dimensional CARS imaging at 2850 cm^{-1} in order to investigate the dynamics of LD fusion in living adipocytes undergoing differentiation.[112] They used the Imaris software package (http://bitplane.com) for detection and tracking of LDs. In Imaris, thresholding is performed for automated segmentation of LDs. Morphological characterization of identified LDs is then performed including radius and volume rendering. Detected LDs are then tracked by selecting for appropriate three-dimensional tracking algorithm. Based on the lipid transfer rates obtained, researchers suggested a model in which lipid transfer is driven by the pressure difference between participating LDs through a putative fusion pore, whose size depends on the size of the donor LD.

Zhang *et al.* used SRS microscopy to study the dynamics of LDs using three-dimensional SRS imaging at 2850 cm^{-1}.[113] They implemented a feature point tracking algorithm, as developed for the Particle Tracker software, [114] for monitoring LD movements. In this software, feature points are localized by finding local intensity maxima in the filtered image. The retrieved positions are then refined to reduce the standard deviation of the position measurement, which takes into consideration a user-provided threshold. Once point location matrices have been defined for each frame in the time-resolved image, a cost function is minimized to find a set of associations for tracking each point. Using this software, researchers demonstrated that the dynamics of LDs, quantified using maximum displacement and speed as the parameters, can be used to differentiate changes in lipid metabolism in living cells. They studied changes in lipid metabolism upon glucose starvation and refeeding and showed that their methodology could predict increase in lipolysis upon starvation as expected.

Analyst Accepted Manuscript

View Article Online
DOI: 10.1039/C8AN01525B

Published on 17 October 2018. Downloaded by University of California - Berkeley on 10/17/2018 9:25:16 PM.

Medyukhina *et al.* developed an image processing approach for detection of nuclear and cellular boundaries from co-registered two-photon excited fluorescence (TPEF) and CARS images respectively.[115] For nuclei boundary determination, they first used the local gray-scale minimum from denoised TPEF images for localization of nuclei centers. The gradient maxima from each nucleus location was used to detect the nuclear boundary. Once nuclei locations and boundaries were validated, they subsequently used TPEF images to delineate the cellular boundaries in the denoised CARS images. They assumed that the cellular boundary corresponds to the first local gradient minimum behind the nuclear boundary. Finally, they demonstrated the implementation of this approach for automated segmentation of cells and nuclei in brain tumor samples.

In order to reveal single-cell heterogeneity, data has to be acquired from multiple single cells for statistically significant conclusions. Cao *et al.* characterized the mechanisms of LD growth and formation upon lipid accumulation, as induced by exogenous FFA, at the single-cell level using SRS microscopy.[116] LD growth and formation was monitored by tracking the number, average size, and average SRS intensity of LDs in a single cell under various concentrations of FFA. To increase throughput and therefore statistical power, all experiments were performed on a microfluidic platform capable of delivering controlled concentration of FFA to uniquely addressable nanoliter cell culture colonies. Images were obtained at 2850 cm^{-1} to identify LDs (Fig. 6A). A second set of images were taken at the protein-rich CH_3 stretching vibration at 2950 cm^{-1} to extract boundaries of single cells. Thresholding was performed to generate a LD and cell mask. The position and morphology of each LD was then recorded and assigned to an individual cell (Fig. 6B). In this investigation, researchers found that lipid accumulation in nonadipocyte cells is mainly reflected in the increase of LD number, as opposed to an increase in their size or lipid concentration.

5. From lipidomic to multiomic analysis

Highly-multiplexed barcoding strategies and automated fluid handling has now made it possible to profile the transcriptome from thousands of single cells in one experiment. However, in order to understand the correlation between gene expression and metabolic states at the single-cell level, multiple measurements must be made on the same single cell. Because CRS imaging in non-destructive, cells can be sequenced directly downstream of lipidomic analysis, thereby making implementation of multi-omic approaches possible. In this section, we will discuss the applicability of utilizing the developed microfluidic and microscopic platforms for combined single-cell genomic and lipidomic analysis.

5.1. Microfluidic Platforms

Microfluidic technology has proven critical for increasing the throughput of NGS techniques permitting profiling of genome-wide features from a large number of single cells. Implementation of single-cell sequencing requires single-cell isolation. In microfluidic platforms, this is typically achieved by valve-based compartmentalization,[117,118] droplet encapsulation,[119,120] and microwell separation.[121,122] After single-cell isolation, downstream library preparation reactions are implemented. Another advantage of microfluidic devices is the optical transparency of the polymer used for chip fabrication, polydimethylsiloxane (PDMS), which enables researchers to visualize sequencing protocols in real-time using a microscope. Because of the optical transparent nature of microfluidic devices and the necessity to physically isolate single cells, lipidomic and genomic analysis can be performed on the same single cell by acquiring images upstream of library preparation reactions (Fig. 7A).

Analyst Accepted Manuscript

View Article Online
DOI: 10.1039/C8AN01525B

Published on 17 October 2018. Downloaded by University of California - Berkeley on 10/17/2018 9:25:16 PM.

Streets *et al.* developed a microfluidic platform for whole-transcriptome profiling of single cells.[118] In this device, cells were isolated in nanoliter-scale trapping chambers using a valve-based strategy. CRS imaging can be performed while cells are trapped thereby allowing researchers to perform combined lipidomic and genomic analysis on the same cell. Lane *et al.* integrated epifluorescence microscopy with scRNA-seq on a commercial microfluidic platform, Fluidigm C1.[123] They used this approach to measure both the dynamics of activation for a specific transcription factor and the global transcriptional response in the same individual cell. Instead of fluorescence microscopy, label-free CRS imaging can be implemented on this platform for combined lipidomic and genomic analysis on the same cell. Gierahn *et al.*[124] and Bose *et al.*[125] developed platforms for massively parallel scRNA-seq based on gravitational settling of single cells in subnanoliter and picoliter-scale microwells respectively. As cells are stationary while isolated in microwells, this solid-phase capture can be utilized for high-resolution CRS imaging upstream of library preparation reactions. Zhang *et al.* developed a flow cytometer based on Raman scattering for fast, high-throughput single-cell analysis.[126] They developed a multiplex stimulated Raman scattering flow cytometry (SRS-FC) technique for measuring chemical contents of single cells. This technique can be extended for quantifying lipid content in single cells. These cells can then be isolated using droplet encapsulation platforms[119,120] for scRNA-seq. Thus coupling SRS-FC with droplet encapsulation-based microfluidic platforms will allow researchers to perform combined lipidomic and genomic analysis on the same cell. Such coupled datasets will transform the way we understand single-cell biology by enabling researchers to study the correlation between single-cell phenotype and gene expression profile.

5.1.1. High-Speed CRS Imaging

Microfluidic devices have enabled researchers to perform single-cell analysis in a high-throughput fashion. In the previous paragraph, we discussed the applicability of microfluidic platforms for retrieving lipidomic (CRS imaging) as well as transcriptomic (scRNA-seq) information from the same single cell, thereby advancing towards multi-omic approaches. However, implementation of such coupled experiments on hundreds to thousands of single cells will require application of high-speed CRS imaging techniques for fast single-cell lipidome profiling. As discussed previously, hyperspectral imaging techniques are essential for profiling the distribution of multiple cellular lipids simultaneously. Thus, it becomes critical to employ hyperspectral CRS techniques capable of rapid spectral acquisition at microsecond scale. Recent developments in CARS and SRS instrumentation have been influential in accelerating the spectral acquisition rate. For example, Liao *et al.* demonstrated parallel acquisition of SRS signal over 180 cm^{-1} bandwidth (~20 spectral data points) with 42 µs pixel dwell time using spectrally focused laser pulses and a homebuilt microsecond optical delay-line tuner.[127] He *et al.* integrated a galvanometer mirror-based rapid-scanning optical delay line with spectrally focused laser pulses to acquire a spectrum with 20 data points in 40 µs.[128] Liao *et al.* built an array of tuned amplifiers for lock-in free parallel acquisition of SRS signal over 180 cm^{-1} bandwidth (~20 spectral data points) with 32 µs pixel dwell time using multiplexed SRS.[129,130] Alshaykh *et al.* integrated a rapid acousto-optic delay line with spectrally focused laser pulses to achieve parallel acquisition of SRS signal over 180 cm^{-1} bandwidth (~20 spectral data points) with 12.8 µs pixel dwell time.[131] Hashimoto *et al.* coupled a rapid-scanning retro-reflective optical path length scanner with a Fourier-transform CARS (FT-CARS) system to accomplish spectral acquisition rate of 20,000 spectra/second over 1300 cm^{-1} bandwidth (~130 spectral data points).[132] Tamamitsu *et al.* updated this system to incorporate a more rapidly scanning optical delay line thereby achieving spectral acquisition rate of 50,000 spectra/sec (~500 spectral data points).[133] Recently, Coluccelli *et al.* demonstrated parallel detection of CARS signal with Raman shifts of ~ 3000 cm^{-1} using FT-CARS. The system was based on a single high-

Analyst Accepted Manuscript

View Article Online
DOI: 10.1039/C8AN01525B

Published on 17 October 2018. Downloaded by University of California - Berkeley on 10/17/2018 9:25:16 PM.

power Yb-fiber laser source coupled to a FT interferometer with pixel dwell time of 160 µs (~675 spectral data points).[134] Thus, such studies focused on development of rapid CRS imaging techniques demonstrate the promise of coupling high-content spectral imaging with high-throughput single-cell analysis.

5.2. Microscopic Platforms

An alternative to physical isolation for single-cell genomic analysis is to employ techniques that turn the genomic information into optical information *in situ*. Fluorescence *in situ* hybridization (FISH) is a technique that uses fluorescent probes that bind specifically to complementary nucleic acid sequences. Thus, researchers can obtain spatial information about the distribution and subcellular localization of specific DNA or RNA molecules. *In-situ* sequencing leverages FISH to extract sequence information from tens to hundreds of targeted transcripts for large scale gene expression profiling in single cells.[135-137] Such methods preserve the microenvironment of the biological sample allowing single molecule RNA sequencing and localization without removing cells from their original context. These emerging technologies are enabling a new-wave of spatial transcriptomic studies, which link single-cell gene expression to cellular niche in a tissue or organ. Since FISH techniques are fundamentally based on imaging, quantitative CRS techniques for lipidomic analysis can be combined with *in situ* sequencing for multi-omic single-cell analysis. Figure 7B illustrates how single-cell transcriptomics might be combined with CRS-based single-cell lipidomics.

6. Conclusion

Coherent Raman scattering (CRS) techniques have become an essential tool for profiling LDs in single-cells by enabling researchers to quantify intracellular lipids in a non-destructive and time-resolved fashion. As the development of CRS instrumentation progresses towards higher specificity, sensitivity, and faster hyperspectral imaging, and next generation sequencing techniques advance towards higher throughput single-cell genomic analysis with lesser bias, coupling these techniques will lead to a more acute understanding of the regulation of metabolic pathways. For example, adipocytes display a wide range of functions and phenotypes, from energy storage in large unilocular LDs (white adipocytes) to thermogenic lipolysis of small LDs (brown adipocytes). Adult humans were thought to only have white adipose tissue with brown adipose tissue being essentially absent after infancy.[138,139] In the early 2000s, observations in the field of nuclear medicine started challenging this notion.[140,141] Multiple studies performing positron emission tomography (PET) with [18F]-fluorodeoxyglucose (FDG) for staging of cancer observed increased uptake of glucose in tumor-unrelated areas.[140,141] These areas were found in the neck and shoulder region and presented itself with features of adipose tissue. It was hypothesized that this FDG uptake could represent activated brown adipose tissue in adult humans and this was finally demonstrated by three independent studies in 2009.[142-144] Now, the existence of brown adipose tissue in adult humans is a well-accepted fact in the research community. Rodents also have a third kind of adipocyte called beige adipocyte, which has a different developmental origin from brown adipocytes.[145] This fact naturally raises the question of whether humans also possess beige adipocytes. Interestingly, recent investigations of human brown adipocytes have reported the mixed presence of presumed beige adipocytes.[146,147] These claims have been reported based on the upregulation of beige adipocyte markers as identified in rodents. Consequently, it is clear that we are only just beginning to understand and appreciate the vast cellular diversity of human adipose tissue. These data raise some critical questions about the composition of human adipose tissue that might only be addressed with single-cell measurements. Technology that couples CRS for lipid profiling and RNA-sequencing for gene expression analysis in single cells could greatly

Analyst Accepted Manuscript

View Article Online
DOI: 10.1039/C8AN01525B

advance our understanding of adipocyte heterogeneity. We anticipate that imaging and sequencing single cells will be the next wave of multi-omic single-cell analysis.

Acknowledgements

This publication was supported by the National Institute of General Medical Sciences of the National Institutes of Health under Award Number R35GM124916. AMS is a Chan Zuckerberg Investigator.

References

1 R. Losick and C. Desplan, *Science*, 2008, **320**, 65–68.
2 G. Guo, M. Huss, G. Q. Tong, C. Wang, L. Li Sun, N. D. Clarke and P. Robson, *Dev. Cell*, 2010, **18**, 675–685.
3 N. Navin, J. Kendall, J. Troge, P. Andrews, L. Rodgers, J. McIndoo, K. Cook, A. Stepansky, D. Levy, D. Esposito, L. Muthuswamy, A. Krasnitz, W. R. McCombie, J. Hicks and M. Wigler, *Nature*, 2011, **472**, 90–95.
4 P. Dalerba, T. Kalisky, D. Sahoo, P. S. Rajendran, M. E. Rothenberg, A. A. Leyrat, S. Sim, J. Okamoto, D. M. Johnston, D. Qian, M. Zabala, J. Bueno, N. F. Neff, J. Wang, A. A. Shelton, B. Visser, S. Hisamori, Y. Shimono, M. Van De Wetering, H. Clevers, M. F. Clarke and S. R. Quake, *Nat. Biotechnol.*, 2011, **29**, 1120–1127.
5 S. J. Altschuler and L. F. Wu, *Cell*, 2010, **141**, 559–563.
6 *Nat. Methods*, 2018, **15**, 299.
7 A. Regev, S. A. Teichmann, E. S. Lander, I. Amit, C. Benoist, E. Birney, B. Bodenmiller, P. Campbell, P. Carninci, M. Clatworthy, H. Clevers, B. Deplancke, I. Dunham, J. Eberwine, R. Eils, W. Enard, A. Farmer, L. Fugger, B. Göttgens, N. Hacohen, M. Haniffa, M. Hemberg, S. Kim, P. Klenerman, A. Kriegstein, E. Lein, S. Linnarsson, E. Lundberg, J. Lundeberg, P. Majumder, J. C. Marioni, M. Merad, M. Mhlanga, M. Nawijn, M. Netea, G. Nolan, D. Pe'er, A. Phillipakis, C. P. Ponting, S. Quake, W. Reik, O. Rozenblatt-Rosen, J. Sanes, R. Satija, T. N. Schumacher, A. Shalek, E. Shapiro, P. Sharma, J. W. Shin, O. Stegle, M. Stratton, M. J. T. Stubbington, F. J. Theis, M. Uhlen, A. Van Oudenaarden, A. Wagner, F. Watt, J. Weissman, B. Wold, R. Xavier and N. Yosef, *Elife*, , DOI:10.7554/eLife.27041.
8 S. Darmanis, S. A. Sloan, Y. Zhang, M. Enge, C. Caneda, L. M. Shuer, M. G. Hayden Gephart, B. A. Barres and S. R. Quake, *Proc. Natl. Acad. Sci. U. S. A.*, 2015, **112**, 7285–90.
9 A. Zeisel, A. B. Moz-Manchado, S. Codeluppi, P. Lönnerberg, G. La Manno, A. Juréus, S. Marques, H. Munguba, L. He, C. Betsholtz, C. Rolny, G. Castelo-Branco, J. Hjerling-Leffler and S. Linnarsson, *Science*, 2015, **347**, 1138–1142.
10 E. M. Kernfeld, R. M. J. Genga, K. Neherin, M. E. Magaletta, P. Xu and R. Maehr, *Immunity*, 2018, **48**, 1258–1270.e6.
11 M. J. Muraro, G. Dharmadhikari, D. Grün, N. Groen, T. Dielen, E. Jansen, L. van Gurp, M. A. Engelse, F. Carlotti, E. J. P. de Koning and A. van Oudenaarden, *Cell Syst.*, 2016, **3**, 385–394.e3.
12 S. R. Quake, T. M. C. The, T. Wyss-Coray and S. Darmanis, *bioRxiv*, 2018, 237446.
13 X. Han, R. Wang, Y. Zhou, L. Fei, H. Sun, S. Lai, A. Saadatpour, Z. Zhou, H. Chen, F. Ye, D. Huang, Y. Xu, W. Huang, M. Jiang, X. Jiang, J. Mao, Y. Chen, C. Lu, J. Xie, Q. Fang, Y. Wang, R. Yue, T. Li, H. Huang, S. H. Orkin, G.-C. Yuan, M. Chen and G. Guo, *Cell*, 2018, **172**, 1091–1107.e17.
14 A. Z. Fernandis and M. R. Wenk, *Curr. Opin. Lipidol.*, 2007, **18**, 121–128.

Published on 17 October 2018. Downloaded by University of California - Berkeley on 10/17/2018 9:25:16 PM.

Analyst Accepted Manuscript

View Article Online
DOI: 10.1039/C8AN01525B

Published on 17 October 2018. Downloaded by University of California - Berkeley on 10/17/2018 9:25:16 PM.

15 H. Sunshine and M. L. Iruela-Arispe, *Curr. Opin. Lipidol.*, 2017, **28**, 408–413.
16 A. Higdon, A. R. Diers, J. Y. Oh, A. Landar and V. M. Darley-Usmar, *Biochem. J.*, 2012, **442**, 453–464.
17 A.-E. Saliba, I. Vonkova and A.-C. Gavin, *Nat. Rev. Mol. Cell Biol.*, 2015, **16**, 753–761.
18 J. P. Ayyappan, A. Paul and Y. H. Goo, *Mol. Med. Rep.*, 2016, **13**, 4527–4534.
19 M. Beller, K. Thiel, P. J. Thul and H. Jäckle, *FEBS Lett.*, 2010, **584**, 2176–2182.
20 M. A. Welte, *Curr. Biol.*, 2015, **25**, R470–R481.
21 K. Bersuker and J. A. Olzmann, *Biochim. Biophys. Acta - Mol. Cell Biol. Lipids*, 2017, **1862**, 1166–1177.
22 S. Kaushik and A. M. Cuervo, *Nat. Cell Biol.*, 2015, **17**, 759–770.
23 S. Yue, J. Li, S. Y. Lee, H. J. Lee, T. Shao, B. Song, L. Cheng, T. A. Masterson, X. Liu, T. L. Ratliff and J. X. Cheng, *Cell Metab.*, 2014, **19**, 393–406.
24 D. K. Nomura, J. Z. Long, S. Niessen, H. S. Hoover, S. W. Ng and B. F. Cravatt, *Cell*, 2010, **140**, 49–61.
25 J. Jo, O. Gavrilova, S. Pack, W. Jou, S. Mullen, A. E. Sumner, S. W. Cushman and V. Periwal, *PLoS Comput. Biol.*, 2009, **5**, e1000324.
26 S. Carobbio, S. Rodriguez-Cuenca and A. Vidal-Puig, *Curr. Opin. Clin. Nutr. Metab. Care*, 2011, **14**, 520–526.
27 E. Levelt, M. Pavlides, R. Banerjee, M. Mahmod, C. Kelly, J. Sellwood, R. Ariga, S. Thomas, J. Francis, C. Rodgers, W. Clarke, N. Sabharwal, C. Antoniades, J. Schneider, M. Robson, K. Clarke, T. Karamitsos, O. Rider and S. Neubauer, *J. Am. Coll. Cardiol.*, 2016, **68**, 53–63.
28 T. K. Smith, T. B. Reynolds and P. W. Denny, *Biochem. Res. Int.*, 2012, **2012**, 1–2.
29 J. W. Yun, *Phytochemistry*, 2010, **71**, 1625–1641.
30 M. Visram, M. Radulovic, S. Steiner, N. Malanovic, T. O. Eichmann, H. Wolinski, G. N. Rechberger and O. Tehlivets, *J. Biol. Chem.*, 2018, **293**, 5544–5555.
31 F. Chiappini, A. Coilly, H. Kadar, P. Gual, A. Tran, C. Desterke, D. Samuel, J. C. Duclos-Vallée, D. Touboul, J. Bertrand-Michel, A. Brunelle, C. Guettier and F. Le Naour, *Sci. Rep.*, 2017, **7**, 46658.
32 H. C. Köfeler, A. Fauland, G. N. Rechberger and M. Trötzmüller, *Metabolites*, 2012, **2**, 19–38.
33 T. Cajka and O. Fiehn, *TrAC - Trends Anal. Chem.*, 2014, **61**, 192–206.
34 L. Li, J. Han, Z. Wang, J. Liu, J. Wei, S. Xiong and Z. Zhao, *Int. J. Mol. Sci.*, 2014, **15**, 10492–10507.
35 M. Wang, C. Wang, R. H. Han and X. Han, *Prog. Lipid Res.*, 2016, **61**, 83–108.
36 X. Han and R. W. Gross, *Mass Spectrom. Rev.*, 2005, **24**, 367–412.
37 N. Tsuyama, H. Mizuno and T. Masujima, *Biol. Pharm. Bull.*, 2012, **35**, 1425–1431.
38 R. Zenobi, *Science (80-.).*, , DOI:10.1126/science.1243259.
39 S. S. Rubakhin, E. J. Lanni and J. V. Sweedler, *Curr. Opin. Biotechnol.*, 2013, **24**, 95–104.
40 L. Zhang and A. Vertes, *Angew. Chemie - Int. Ed.*, 2018, **57**, 4466–4477.
41 K. J. Boggio, E. Obasuyi, K. Sugino, S. B. Nelson, N. Y. R. Agar and J. N. Agar, *Expert Rev. Proteomics*, 2011, **8**, 591–604.
42 E. J. Lanni, S. S. Rubakhin and J. V. Sweedler, *J. Proteomics*, 2012, **75**, 5036–5051.
43 N. Goto-Inoue, T. Hayasaka, N. Zaima and M. Setou, *Biochim. Biophys. Acta - Mol. Cell Biol. Lipids*, 2011, **1811**, 961–969.
44 D. Touboul, A. Brunelle and O. Laprévote, *Biochimie*, 2011, **93**, 113–119.
45 D. Gode and D. A. Volmer, *Analyst*, 2013, **138**, 1289–1315.
46 A. Römpp and B. Spengler, *Histochem. Cell Biol.*, 2013, **139**, 759–783.
47 J. Pól, M. Strohalm, V. Havlíček and M. Volný, *Histochem. Cell Biol.*, 2010, **134**, 423–443.
48 S. J. Blanksby and T. W. Mitchell, *Annu. Rev. Anal. Chem.*, 2010, **3**, 433–465.

Analyst Accepted Manuscript

View Article Online
DOI: 10.1039/C8AN01525B

Published on 17 October 2018. Downloaded by University of California - Berkeley on 10/17/2018 9:25:16 PM.

49 M. Maekawa and G. D. Fairn, *J. Cell Sci.*, 2014, **127**, 4801–4812.
50 S. Daemen, M. A. M. J. van Zandvoort, S. H. Parekh and M. K. C. Hesselink, *Mol. Metab.*, 2016, **5**, 153–163.
51 K. Yen, T. T. Le, A. Bansal, S. D. Narasimhan, J. X. Cheng and H. A. Tissenbaum, *PLoS One*, 2010, **5**, 1–10.
52 J. K. Sims, B. Rohr, E. Miller and K. Lee, *Tissue Eng. Part C Methods*, 2015, **21**, 605–613.
53 C. I. McPhee, G. Zoriniants, W. Langbein and P. Borri, *Biophys. J.*, 2013, **105**, 1414–20.
54 K. Kim, S. Lee, J. Yoon, J. Heo, C. Choi and Y. Park, *Sci. Rep.*, , DOI:10.1038/srep36815.
55 D. Débarre, W. Supatto, A.-M. Pena, A. Fabre, T. Tordjmann, L. Combettes, M.-C. Schanne-Klein and E. Beaurepaire, *Nat. Methods*, 2006, **3**, 47–53.
56 T. A. Bley, O. Wieben, C. J. Fran??ois, J. H. Brittain and S. B. Reeder, *J. Magn. Reson. Imaging*, 2010, **31**, 4–18.
57 J.-H. Hwang and C. S. Choi, *Exp. Mol. Med.*, 2015, **47**, e139.
58 K. Jurowski, K. Kochan, J. Walczak, M. Barańska, W. Piekoszewski and B. Buszewski, *Crit. Rev. Anal. Chem.*, 2017, **47**, 418–437.
59 J. X. Cheng, Y. K. Jia, G. Zheng and X. S. Xie, *Biophys. J.*, 2002, **83**, 502–509.
60 C. W. Freudiger, W. Min, B. G. Saar, S. Lu, G. R. Holtom, C. He, J. C. Tsai, J. X. Kang and X. S. Xie, *Science (80-.).*, 2008, **322**, 1857–1861.
61 a Schönle and S. W. Hell, *Opt. Lett.*, 1998, **23**, 325–327.
62 R. Galli, O. Uckermann, E. F. Andresen, K. D. Geiger, E. Koch, G. Schackert, G. Steiner and M. Kirsch, *PLoS One*, 2014, **9**, e110295.
63 X. Nan, E. O. Potma and X. S. Xie, *Biophys. J.*, 2006, **91**, 728–735.
64 L. Gao, H. Zhou, M. J. Thrall, F. Li, Y. Yang, Z. Wang, P. Luo, K. K. Wong, G. S. Palapattu and S. T. C. Wong, *Biomed. Opt. Express*, 2011, **2**, 915.
65 F.-K. Lu, S. Basu, V. Igras, M. P. Hoang, M. Ji, D. Fu, G. R. Holtom, V. A. Neel, C. W. Freudiger, D. E. Fisher and X. S. Xie, *Proc. Natl. Acad. Sci. U. S. A.*, 2015, **112**, 11624–9.
66 D. Zhang, M. N. Slipchenko and J. X. Cheng, *J. Phys. Chem. Lett.*, 2011, **2**, 1248–1253.
67 Y. Fu, H. Wang, R. Shi and J.-X. Cheng, *Opt. Express*, 2006, **14**, 3942.
68 A. Hopt and E. Neher, *Biophys. J.*, 2001, **80**, 2029–2036.
69 K. Konig, U. Simon and K. J. Halbhuber, *Cell. Mol. Biol.*, 1996, **42**, 1181–1194.
70 K. König, P. T. C. So, W. W. Mantulin and E. Gratton, *Opt. Lett.*, 1997, **22**, 135.
71 W. W. Chen, C. H. Chien, C. L. Wang, H. H. Wang, Y. L. Wang, S. T. Ding, T. S. Lee and T. C. Chang, *Anal. Bioanal. Chem.*, 2013, **405**, 8549–8559.
72 H. A. Rinia, K. N. J. Burger, M. Bonn and M. Müller, *Biophys. J.*, 2008, **95**, 4908–4914.
73 M. C. Wang, W. Min, C. W. Freudiger, G. Ruvkun and X. S. Xie, *Nat. Methods*, 2011, **8**, 135–138.
74 T. T. Le, S. Yue and J.-X. Cheng, *J. Lipid Res.*, 2010, **51**, 3091–3102.
75 Y. Yu, P. V. Ramachandran and M. C. Wang, *Biochim. Biophys. Acta - Mol. Cell Biol. Lipids*, 2014, **1841**, 1120–1129.
76 X. Nan, J.-X. Cheng and X. S. Xie, *J. Lipid Res.*, 2003, **44**, 2202–2208.
77 T. T. Le and J. X. Cheng, *PLoS One*, 2009, **4**, e5189.
78 H.-J. van Manen, Y. M. Kraan, D. Roos and C. Otto, *Proc. Natl. Acad. Sci. USA*, 2005, **102**, 10159–10164.
79 X. S. Xie, J. Yu and W. Y. Yang, *Science (80-.).*, 2006, **312**, 228–230.
80 H. Yamakoshi, K. Dodo, M. Okada, J. Ando, A. Palonpon, K. Fujita, S. Kawata and M. Sodeoka, *J. Am. Chem. Soc.*, 2011, **133**, 6102–6105.
81 H. Yamakoshi, K. Dodo, A. Palonpon, J. Ando, K. Fujita, S. Kawata and M. Sodeoka, *J. Am. Chem. Soc.*, 2012, **134**, 20681–20689.

Analyst Accepted Manuscript

View Article Online
DOI: 10.1039/C8AN01525B

Published on 17 October 2018. Downloaded by University of California - Berkeley on 10/17/2018 9:25:16 PM.

82 L. Wei, F. Hu, Y. Shen, Z. Chen, Y. Yu, C.-C. Lin, M. C. Wang and W. Min, *Nat. Methods*, 2014, **11**, 410–2.
83 J. Li and J.-X. Cheng, *Sci. Rep.*, 2015, **4**, 6807.
84 F. Hu, Z. Chen, L. Zhang, Y. Shen, L. Wei and W. Min, *Angew. Chemie - Int. Ed.*, 2015, **54**, 9821–9825.
85 E. R. Andresen, P. Berto and H. Rigneault, *Opt. Lett.*, 2011, **36**, 2387.
86 H. T. Beier, G. D. Noojin and B. A. Rockwell, *Opt. Express*, 2011, **19**, 18885.
87 D. Fu, G. Holtom, C. Freudiger, X. Zhang and X. S. Xie, *J. Phys. Chem. B*, 2013, **117**, 4634–4640.
88 D. Zhang, P. Wang, M. N. Slipchenko, D. Ben-Amotz, A. M. Weiner and J.-X. Cheng, *Anal. Chem.*, 2013, **85**, 98–106.
89 J. Li, S. Condello, J. Thomes-Pepin, X. Ma, Y. Xia, T. D. Hurley, D. Matei and J. X. Cheng, *Cell Stem Cell*, 2017, **20**, 303–314.e5.
90 A. Alfonso-García, S. G. Pfisterer, H. Riezman, E. Ikonen and E. O. Potma, *J. Biomed. Opt.*, 2015, **21**, 061003.
91 F. B. Kraemer, *Mol. Cell. Endocrinol.*, 2007, **265–266**, 42–45.
92 V. K. Khor, R. Ahrends, Y. Lin, W. J. Shen, C. M. Adams, A. N. Roseman, Y. Cortez, M. N. Teruel, S. Azhar and F. B. Kraemer, *PLoS One*, 2014, **9**, e105047.
93 D. Fu, Y. Yu, A. Folick, E. Currie, R. V. Farese, T. H. Tsai, X. S. Xie and M. C. Wang, *J. Am. Chem. Soc.*, 2014, **136**, 8820–8828.
94 N. Otsu, *IEEE Trans. Syst. Man. Cybern.*, 1979, **SMC-9**, 62–66.
95 A. dos Anjos and H. Shahbazkia, in *Proc. of ICBED, BIOSIGNALS*, 2008, vol. 2, pp. 70–76.
96 R. Szeliski, Computer Vision: Algorithms and Applications (Texts in Computer Science), Springer, London, 2011.
97 J. Canny, *IEEE Trans. Pattern Anal. Mach. Intell.*, 1986, **PAMI-8**, 679–698.
98 P. Hough, US Pat., US3069654A, 1962.
99 D. H. Ballard, *Pattern Recognit.*, 1981, **13**, 111–122.
100 S. Beucher and C. Lantuejoul, *Int. Work. Image Process. Real-time Edge Motion Detect.*, 1979, 12–21.
101 J. Schindelin, I. Arganda-Carreras, E. Frise, V. Kaynig, M. Longair, T. Pietzsch, S. Preibisch, C. Rueden, S. Saalfeld, B. Schmid, J. Y. Tinevez, D. J. White, V. Hartenstein, K. Eliceiri, P. Tomancak and A. Cardona, *Nat. Methods*, 2012, 9, 676–682.
102 S. Y. Dejgaard and J. F. Presley, *J. Histochem. Cytochem.*, 2014, **62**, 889–901.
103 H. Varinli, M. J. Osmond-McLeod, P. L. Molloy and P. Vallotton, *J. Lipid Res.*, 2015, **56**, 2206–2216.
104 K. Fukushima, *Biol Cybern*, 1980, **36**, 193–202.
105 Y. LeCun, L. Bottou, Y. Bengio and P. Haffner, *Proc. IEEE*, 1998, **86**, 2278–2323.
106 G. Litjens, T. Kooi, B. E. Bejnordi, A. A. A. Setio, F. Ciompi, M. Ghafoorian, J. A. W. M. van der Laak, B. van Ginneken and C. I. Sánchez, *Med. Image Anal.*, 2017, 42, 60–88.
107 P. Eulenberg, N. Köhler, T. Blasi, A. Filby, A. E. Carpenter, P. Rees, F. J. Theis and F. A. Wolf, *Nat. Commun.*, , DOI:10.1038/s41467-017-00623-3.
108 C. L. Chen, A. Mahjoubfar, L. C. Tai, I. K. Blaby, A. Huang, K. R. Niazi and B. Jalali, *Sci. Rep.*, , DOI:10.1038/srep21471.
109 D. Fu and X. S. Xie, *Anal. Chem.*, 2014, **86**, 4115–4119.
110 C. Di Napoli, I. Pope, F. Masia, W. Langbein, P. Watson and P. Borri, *Anal. Chem.*, 2016, **88**, 3677–3685.
111 F. Masia, A. Glen, P. Stephens, P. Borri and W. Langbein, *Anal. Chem.*, 2013, **85**, 10820–10828.

Analyst Accepted Manuscript

View Article Online
DOI: 10.1039/C8AN01525B

Published on 17 October 2018. Downloaded by University of California - Berkeley on 10/17/2018 9:25:16 PM.

112 C. Jüngst, M. Klein and A. Zumbusch, *J. Lipid Res.*, 2013, **54**, 3419–3429.
113 C. Zhang, J. Li, L. Lan and J. X. Cheng, *Anal. Chem.*, 2017, **89**, 4502–4507.
114 I. F. Sbalzarini and P. Koumoutsakos, *J. Struct. Biol.*, 2005, **151**, 182–195.
115 A. Medyukhina, T. Meyer, M. Schmitt, B. F. M. Romeike, B. Dietzek and J. Popp, *J. Biophotonics*, 2012, **5**, 878–888.
116 C. Cao, D. Zhou, T. Chen, A. M. Streets and Y. Huang, *Anal. Chem.*, 2016, **88**, 4931–4939.
117 Y. Marcy, C. Ouverney, E. M. Bik, T. Losekann, N. Ivanova, H. G. Martin, E. Szeto, D. Platt, P. Hugenholtz, D. A. Relman and S. R. Quake, *Proc. Natl. Acad. Sci.*, 2007, **104**, 11889–11894.
118 A. M. Streets, X. Zhang, C. Cao, Y. Pang, X. Wu, L. Xiong, L. Yang, Y. Fu, L. Zhao, F. Tang and Y. Huang, *Proc. Natl. Acad. Sci.*, 2014, **111**, 7048–7053.
119 E. Z. Macosko, A. Basu, R. Satija, J. Nemesh, K. Shekhar, M. Goldman, I. Tirosh, A. R. Bialas, N. Kamitaki, E. M. Martersteck, J. J. Trombetta, D. A. Weitz, J. R. Sanes, A. K. Shalek, A. Regev and S. A. McCarroll, *Cell*, 2015, **161**, 1202–1214.
120 A. M. Klein, L. Mazutis, I. Akartuna, N. Tallapragada, A. Veres, V. Li, L. Peshkin, D. A. Weitz and M. W. Kirschner, *Cell*, 2015, **161**, 1187–1201.
121 H. C. Fan, G. K. Fu and S. P. A. Fodor, *Science (80-.).*, , DOI:10.1126/science.1258367.
122 J. Yuan and P. A. Sims, *Sci. Rep.*, , DOI:10.1038/srep33883.
123 K. Lane, D. Van Valen, M. M. DeFelice, D. N. Macklin, T. Kudo, A. Jaimovich, A. Carr, T. Meyer, D. Pe'er, S. C. Boutet and M. W. Covert, *Cell Syst.*, 2017, **4**, 458–469.e5.
124 T. M. Gierahn, M. H. Wadsworth, T. K. Hughes, B. D. Bryson, A. Butler, R. Satija, S. Fortune, J. Christopher Love and A. K. Shalek, *Nat. Methods*, 2017, **14**, 395–398.
125 S. Bose, Z. Wan, A. Carr, A. H. Rizvi, G. Vieira, D. Pe'er and P. A. Sims, *Genome Biol.*, 2015, **16**, 120.
126 C. Zhang, K.-C. Huang, B. Rajwa, J. Li, S. Yang, H. Lin, C. Liao, G. Eakins, S. Kuang, V. Patsekin, J. P. Robinson and J.-X. Cheng, *Optica*, 2017, **4**, 103.
127 C.-S. Liao, K.-C. Huang, W. Hong, A. J. Chen, C. Karanja, P. Wang, G. Eakins and J.-X. Cheng, *Optica*, 2016, **3**, 1377.
128 R. He, Z. Liu, Y. Xu, W. Huang, H. Ma and M. Ji, *Opt. Lett.*, 2017, **42**, 659.
129 C.-S. Liao, M. N. Slipchenko, P. Wang, J. Li, S.-Y. Lee, R. A. Oglesbee and J.-X. Cheng, *Light Sci. Appl.*, 2015, **4**, e265.
130 M. N. Slipchenko, R. A. Oglesbee, D. Zhang, W. Wu and J. X. Cheng, *J. Biophotonics*, 2012, **5**, 801–807.
131 M. S. Alshaykh, C.-S. Liao, O. E. Sandoval, G. Gitzinger, N. Forget, D. E. Leaird, J.-X. Cheng and A. M. Weiner, *Opt. Lett.*, 2017, **42**, 1548.
132 K. Hashimoto, M. Takahashi, T. Ideguchi and K. Goda, *Sci. Rep.*, 2016, **6**, 21036.
133 M. Tamamitsu, Y. Sakaki, T. Nakamura, G. K. Podagatlapalli, T. Ideguchi and K. Goda, *Vib. Spectrosc.*, 2017, **91**, 163–169.
134 N. Coluccelli, E. Vicentini, A. Gambetta, C. R. Howle, K. Mcewan, P. Laporta and G. Galzerano, *Opt. Express*, 2018, **26**, 18855.
135 K. H. Chen, A. N. Boettiger, J. R. Moffitt, S. Wang and X. Zhuang, *Science (80-.).*, , DOI:10.1126/science.aaa6090.
136 J. H. Lee, E. R. Daugharthy, J. Scheiman, R. Kalhor, T. C. Ferrante, R. Terry, B. M. Turczyk, J. L. Yang, H. S. Lee, J. Aach, K. Zhang and G. M. Church, *Nat. Protoc.*, 2015, **10**, 442–458.
137 E. Lubeck, A. F. Coskun, T. Zhiyentayev, M. Ahmad and L. Cai, *Nat. Methods*, 2014, **11**, 360–361.
138 S. Cunningham, P. Leslie, D. Hopwood, P. Illingworth, R. T. Jung, D. G. Nicholls, N. Peden, J. Rafael and E. Rial, *Clin. Sci. (Lond).*, 1985, **69**, 343–8.
139 M. E. Lean, *Proc. Nutr. Soc.*, 1989, **48**, 243–56.

Analyst Accepted Manuscript

View Article Online
DOI: 10.1039/C8AN01525B

140 T. F. Hany, E. Gharehpapagh, E. M. Kamel, A. Buck, J. Himms-Hagen and G. K. von Schulthess, *Eur. J. Nucl. Med. Mol. Imaging*, 2002, **29**, 1393–1398.
141 J. Nedergaard, T. Bengtsson and B. Cannon, *Am. J. Physiol. Metab.*, 2007, **293**, E444–E452.
142 K. A. Virtanen, M. E. Lidell, J. Orava, M. Heglind, R. Westergren, T. Niemi, M. Taittonen, J. Laine, N.-J. Savisto, S. Enerbäck and P. Nuutila, *N. Engl. J. Med.*, 2009, **360**, 1518–1525.
143 W. D. van Marken Lichtenbelt, J. W. Vanhommerig, N. M. Smulders, J. M. A. F. L. Drossaerts, G. J. Kemerink, N. D. Bouvy, P. Schrauwen and G. J. J. Teule, *N. Engl. J. Med.*, 2009, **360**, 1500–1508.
144 A. M. Cypess, S. Lehman, G. Williams, I. Tal, D. Rodman, A. B. Goldfine, F. C. Kuo, E. L. Palmer, Y. H. Tseng, A. Doria, G. M. Kolodny and C. Ronald Kahn, *Obstet. Gynecol. Surv.*, 2009, **64**, 519–520.
145 P. Seale, B. Bjork, W. Yang, S. Kajimura, S. Chin, S. Kuang, A. Scimè, S. Devarakonda, H. M. Conroe, H. Erdjument-Bromage, P. Tempst, M. A. Rudnicki, D. R. Beier and B. M. Spiegelman, *Nature*, 2008, **454**, 961–967.
146 J. Wu, P. Boström, L. M. Sparks, L. Ye, J. H. Choi, A.-H. Giang, M. Khandekar, K. A. Virtanen, P. Nuutila, G. Schaart, K. Huang, H. Tu, W. D. van Marken Lichtenbelt, J. Hoeks, S. Enerbäck, P. Schrauwen and B. M. Spiegelman, *Cell*, 2012, **150**, 366–76.
147 A. M. Cypess, A. P. White, C. Vernochet, T. J. Schulz, R. Xue, C. A. Sass, T. L. Huang, C. Roberts-Toler, L. S. Weiner, C. Sze, A. T. Chacko, L. N. Deschamps, L. M. Herder, N. Truchan, A. L. Glasgow, A. R. Holman, A. Gavrila, P.-O. Hasselgren, M. A. Mori, M. Molla and Y.-H. Tseng, *Nat. Med.*, 2013, **19**, 635–9.

Published on 17 October 2018. Downloaded by University of California - Berkeley on 10/17/2018 9:25:16 PM.

Analyst Accepted Manuscript

View Article Online
DOI: 10.1039/C8AN01525B

Published on 17 October 2018. Downloaded by University of California - Berkeley on 10/17/2018 9:25:16 PM.

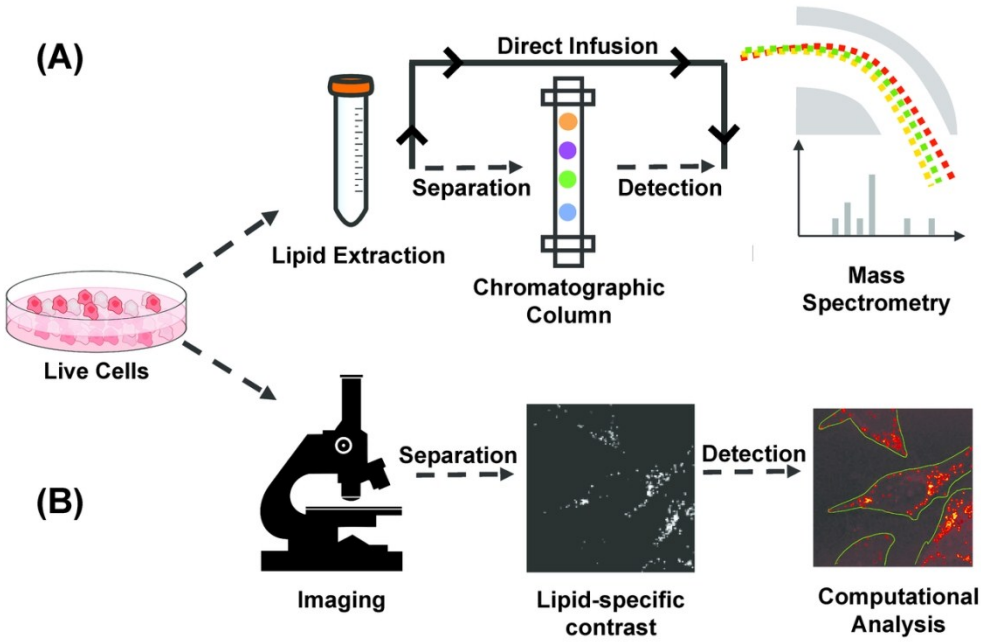

Figure 1. Pipeline of mass spectrometry (MS) and microscopic quantitative imaging for lipidomic analysis (a) In MS-based techniques, lipid is extracted from bulk cells. Extracted lipid can be separated using a gas/liquid chromatographic column before mass spectrometric detection, or directly infused in mass spectrometer for untargeted detection. (b) In quantitative imaging-based techniques, multiple live cells in the field of view are first imaged non-destructively to generate a lipid-specific contrast. The image is then computationally analyzed to segment cells and quantify properties of subcellular lipid droplets on the single-cell level.

110x71mm (300 x 300 DPI)

Analyst Accepted Manuscript

View Article Online
DOI: 10.1039/C8AN01525B

Published on 17 October 2018. Downloaded by University of California - Berkeley on 10/17/2018 9:25:16 PM.

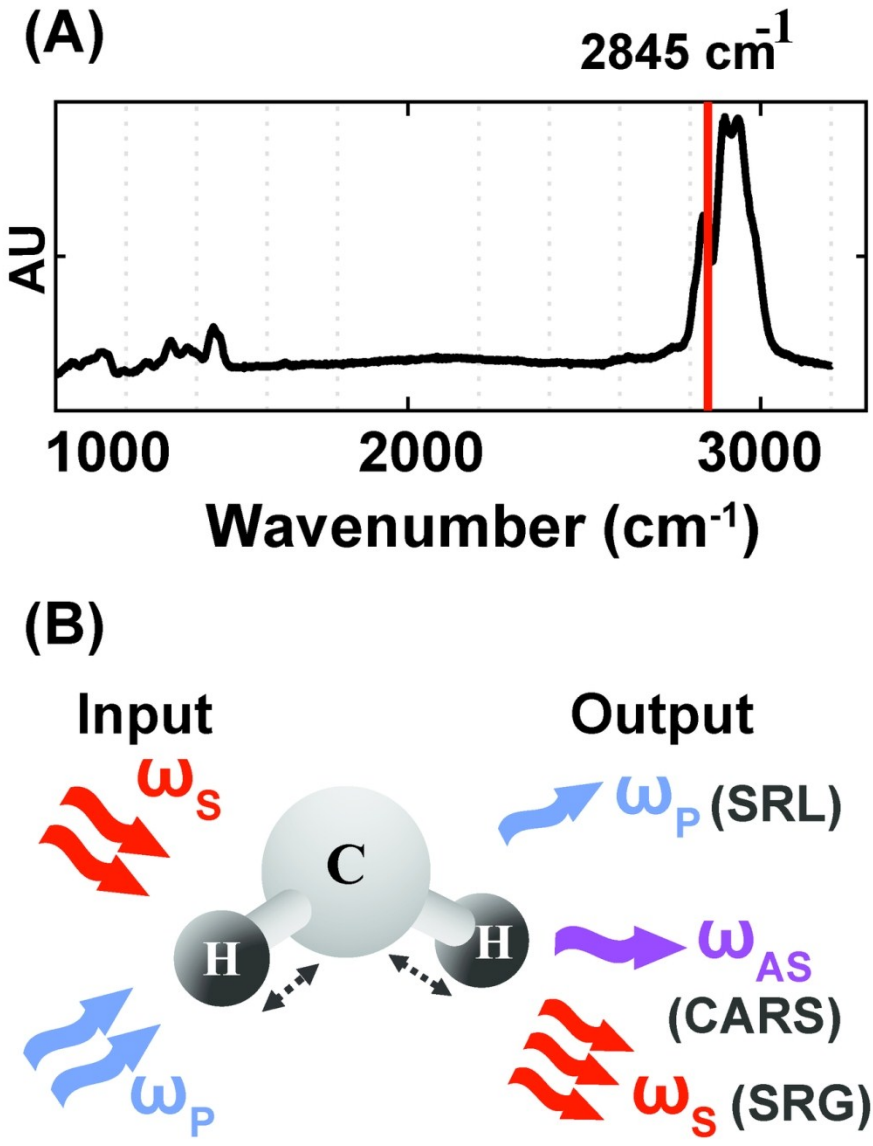

Figure 2. Vibrational imaging of lipids using coherent Raman scattering. (A) Spontaneous Raman spectra of oleic acid. The red solid line indicates asymmetric stretching vibrational mode of the carbon–hydrogen bond at 2,845 cm-1. (B) Schematic of excitation and detection for coherent Raman scattering. For both coherent anti-Stokes Raman scattering (CARS) and stimulated Raman scattering (SRS)imaging, a characteristic vibrational mode of the CH2 bond in lipids is excited with two incoming photons at the pump (ωp) and Stokes (ωs) frequency. Stimulated Raman loss (SRL) is detected as a loss in the pump intensity and stimulated Raman gain (SRG) is detected as a gain in the Stokes intensity. CARS is detected at the anti-Stokes frequency, ωAS.

112x153mm (300 x 300 DPI)

Analyst Accepted Manuscript

View Article Online
DOI: 10.1039/C8AN01525B

Published on 17 October 2018. Downloaded by University of California - Berkeley on 10/17/2018 9:25:16 PM.

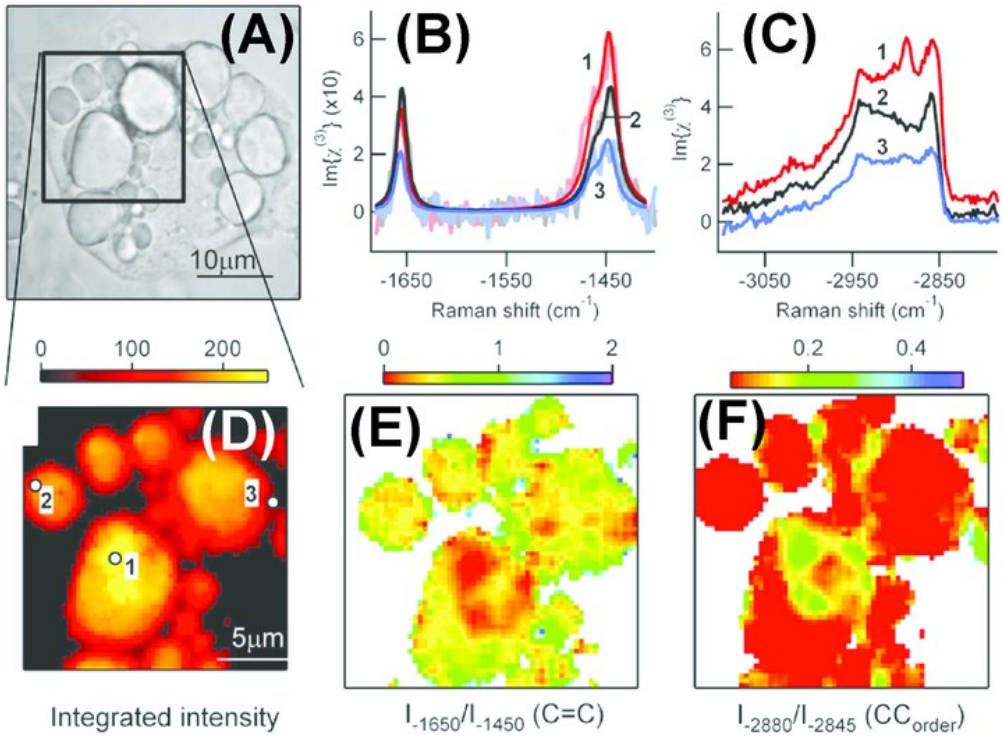

Figure 3. Multiplex coherent anti-Stokes Raman scattering (CARS) imaging of 3T3-L1-derived adipocyte to map the composition and packing of individual lipid droplets. Cells were incubated in a 1:3 mix of unsaturated : saturated fatty acid (A) Brightfield image of an adipocyte. Spontaneous Raman-like spectra in the (B) CC-stretch and (C) CH-stretch regions for locations indicated (in D). Retrieved spectra was then analyzed for mapping the (D) lipid concentration, (E) acyl chain unsaturation and (F) acyl chain order on the same adipocyte. Reprinted from Biophysical Journal, Volume 95, Issue 10, H. A. Rinia, K. N. J. Burger, M. Bonn and M. Müller, Quantitative Label-Free Imaging of Lipid Composition and Packing of Individual Cellular Lipid Droplets Using Multiplex CARS Microscopy, Pages 4908-4914, Copyright (2018), with permission from Elsevier.

60x44mm (300 x 300 DPI)

Analyst Accepted Manuscript

View Article Online
DOI: 10.1039/C8AN01525B

Published on 17 October 2018. Downloaded by University of California - Berkeley on 10/17/2018 9:25:16 PM.

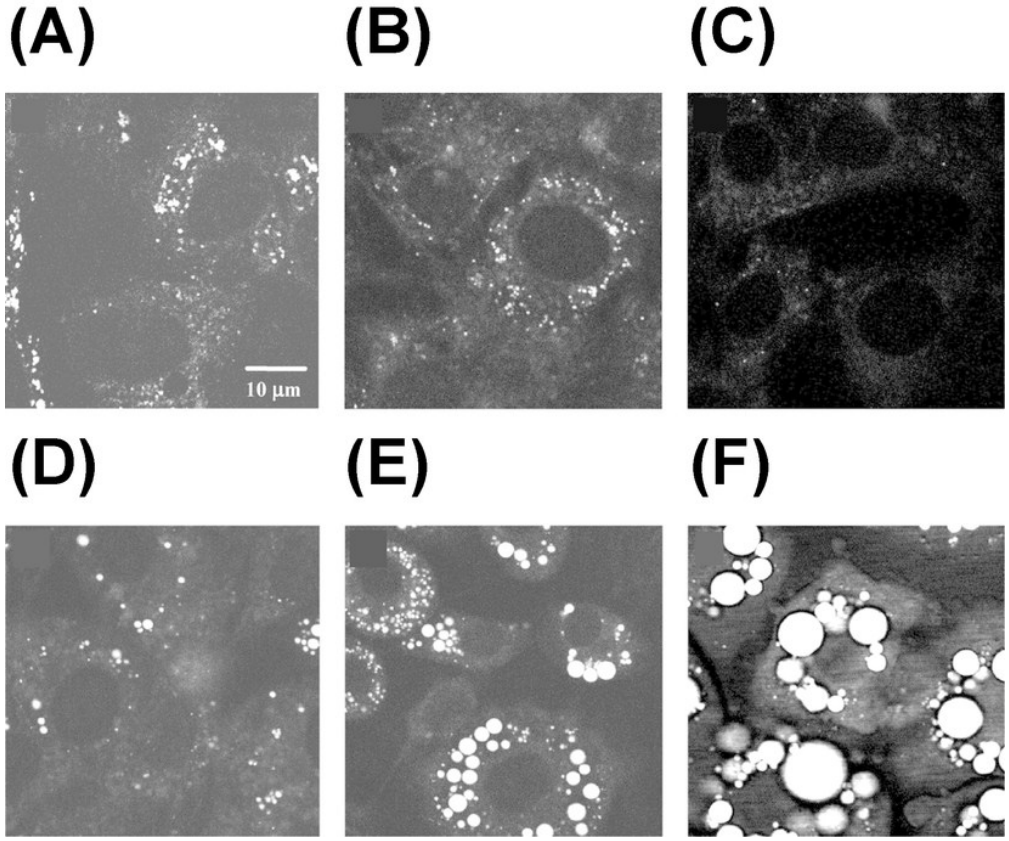

Figure 4. Monitoring lipid droplet formation during differentiation of 3T3-L1 cells using CARS at 2845 cm-1. Images were taken at different times after adding differentiation induction media: (A) 0 h, (B) 24 h, (C) 48 h, (D) 60 h, (E) 96 h, and (F) 192 h. Republished with permission of American Soc for Biochemistry & Molecular Biology, from Vibrational imaging of lipid droplets in live fibroblast cells with coherent anti-Stokes Raman scattering microscopy, X. Nan, J.-X. Cheng and X. S. Xie, volume 44, edition 11, Copyright (2018); permission conveyed through Copyright Clearance Center, Inc.

69x58mm (300 x 300 DPI)

Analyst Accepted Manuscript

View Article Online
DOI: 10.1039/C8AN01525B

Published on 17 October 2018. Downloaded by University of California - Berkeley on 10/17/2018 9:25:16 PM.

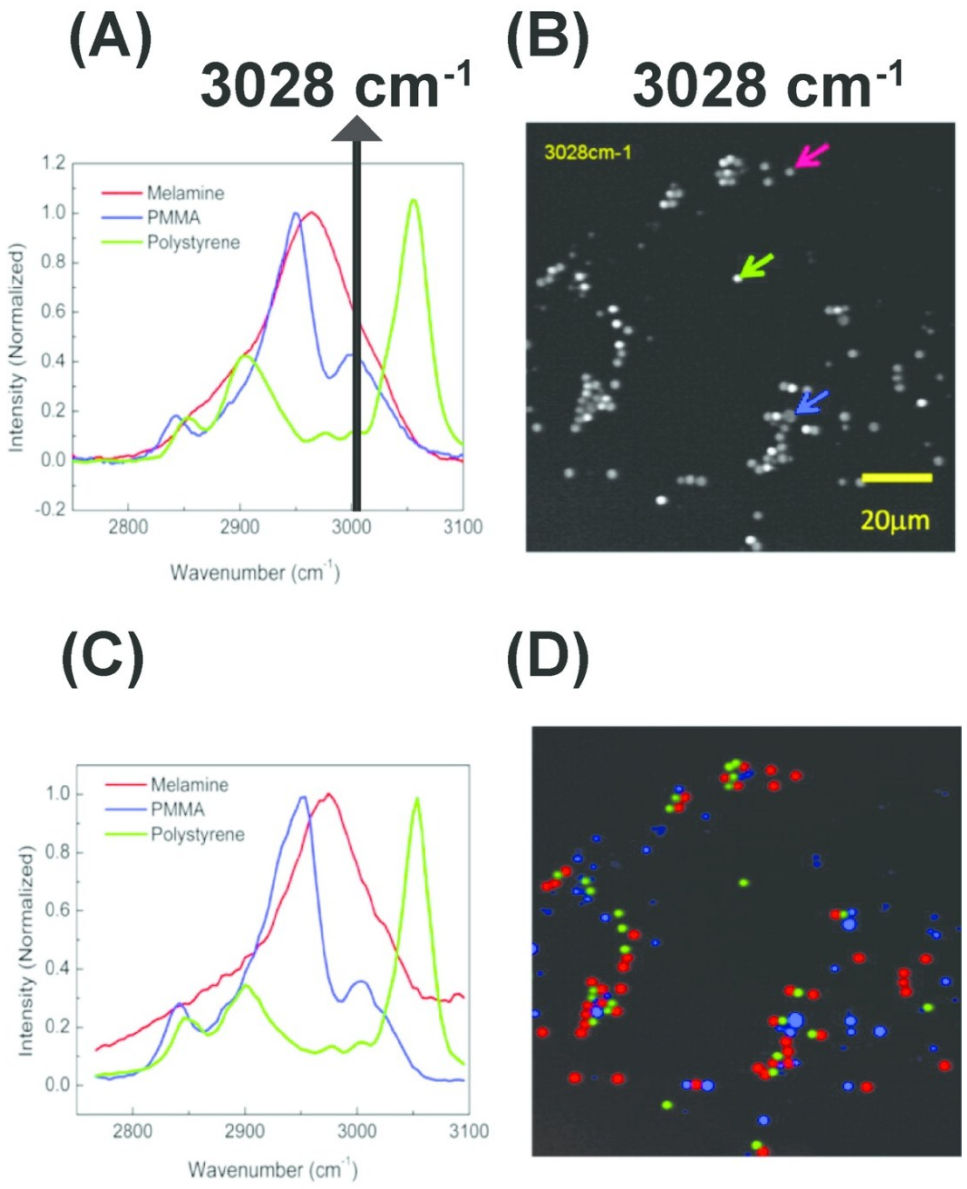

Figure 5. Hyperspectral stimulated Raman scattering (hSRS) imaging for mapping three types of polymer beads with overlapping but distinct Raman spectra (A) Spontaneous Raman spectra of the three polymer beads. The black solid line indicates overlapping Raman spectra at 3028 cm-1 (B) stimulated Raman scattering (SRS) imaging of the three polymer beads at 3028 cm-1 with different color arrows pointing out corresponding beads (C) SRS spectra for the three polymer beads pointed out by the arrows (in B). (D) Color-code distribution of the three polymer beads generated using hSRS imaging coupled with spectral decomposition. PMMA: Poly (methyl methacrylate). Reprinted with permission from D. Fu, G. Holtom, C. Freudiger, X. Zhang and X. S. Xie, J. Phys. Chem. B, 2013, 117, 4634–4640 Copyright (2018) American Chemical Society.

102x126mm (300 x 300 DPI)

Analyst Accepted Manuscript

View Article Online
DOI: 10.1039/C8AN01525B

Published on 17 October 2018. Downloaded by University of California - Berkeley on 10/17/2018 9:25:16 PM.

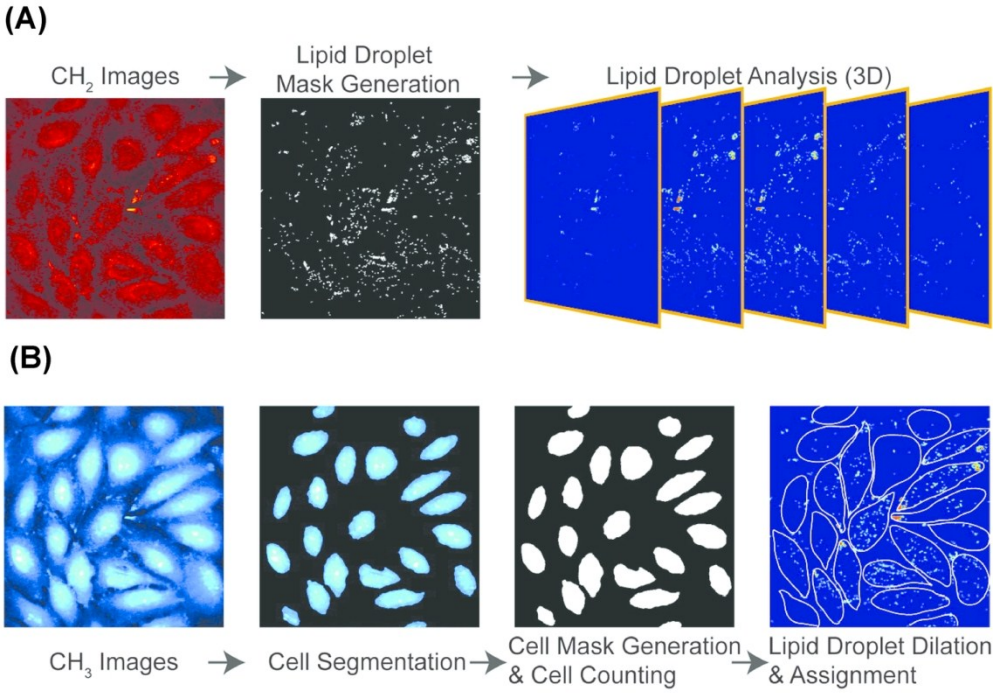

Figure 6. Stimulated Raman scattering (SRS) image processing pipeline for determining cellular boundaries and characterizing lipid droplets in single cells. (A) three-dimensional lipid-specific images were acquired at 2850 cm–1. The signal was processed to generate a lipid droplet mask. The lipid droplet mask was analyzed for three-dimensional morphological characterization (B) three-dimensional protein-specific images were acquired at 2950 cm–1 for cell boundary segmentation and cell mask generation. The position of each LD was then recorded and assigned to an individual cell. Reprinted with permission from C. Cao, D. Zhou, T. Chen, A. M. Streets and Y. Huang, Anal. Chem., 2016, 88, 4931–4939 Copyright (2018) American Chemical Society.

130x98mm (300 x 300 DPI)

Analyst Accepted Manuscript

View Article Online
DOI: 10.1039/C8AN01525B

Published on 17 October 2018. Downloaded by University of California - Berkeley on 10/17/2018 9:25:16 PM.

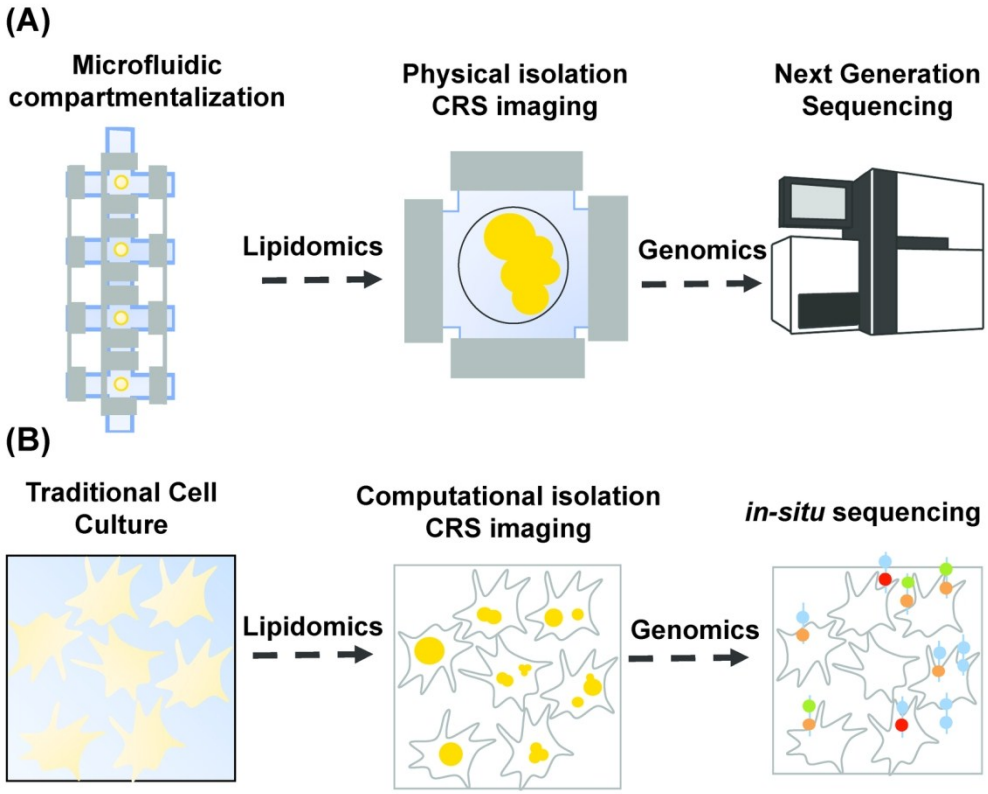

Figure 7. Combining lipidomic and genomic analysis at the single-cell level. (A)Lipidomic and genomic analysis using microfluidic single-cell isolation. A single cell is physically isolated in a small chamber using valve-based compartmentalization. While the cell is trapped, images are acquired in a non-destructive fashion using coherent Raman scattering (CRS) imaging for lipidomic analysis. The cell is then pushed downstream for library preparation and finally sequenced using next generation sequencing (NGS) techniques. (B) Lipidomic and genomic analysis using microscopy and computational cell-segmentation. Multiple live cells are imaged on a coverglass using CRS. Individual cells are then computationally isolated using object recognition algorithms and images are analyzed for lipidomic analysis at the single-cell level. The transcriptome of the same cells is then profiled using in-situ sequencing techniques.

143x119mm (300 x 300 DPI)

Analyst Accepted Manuscript

View Article Online
DOI: 10.1039/C8AN01525B

Non-destructive spatial characterization of lipid droplets using coherent Raman scattering microscopy and computational image analysis algorithms at the single-cell level

Published on 17 October 2018. Downloaded by University of California - Berkeley on 10/17/2018 9:25:16 PM.

Analyst Accepted Manuscript

View Article Online
DOI: 10.1039/C8AN01525B

Published on 17 October 2018. Downloaded by University of California - Berkeley on 10/17/2018 9:25:16 PM.

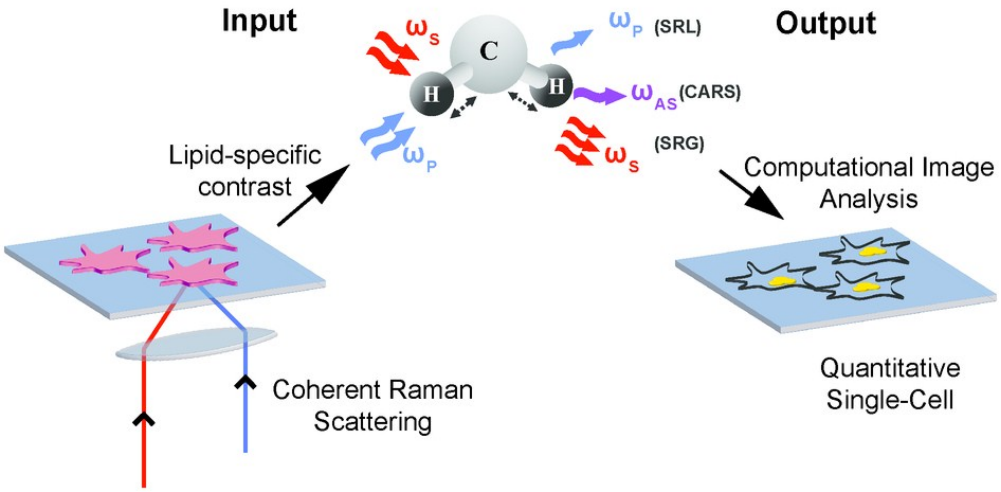

80x40mm (300 x 300 DPI)

Analyst Accepted Manuscript